Revision 1

Surface specific measurements of olivine dissolution by phase-shift interferometry

Helen E. King[1], Hisao Satoh[2,3], Katsuo Tsukamoto[2] and Andrew Putnis[1]

[1]Institut für Mineralogie, University of Münster, Germany; [2]Department of Earth and Planetary Materials Science, Tohoku University, Japan; [3]Mitsubishi Materials Corporation, Japan

Abstract

Natural olivine dissolution and replacement often occurs preferentially along specific crystallographic planes. Thus, olivine reactivity at specific surfaces was examined in situ using phase-shift interferometry, which has a detection limit $<10^{-5}$ nm/sec, by dissolving two smoothed olivine crystal faces and a third sample corresponding to a surface that was generated by preferential dissolution along structural defects. The experiments were conducted at 22 °C and ambient pressure in 0.1 M NaCl solutions that were acidified to pHs between 1 and 4 using 0.1 M HCl. These experiments show that olivine dissolution can vary from one surface to another as well as in different areas of the same surface that have similar characteristics. The fastest vertical retreat occurred at the surfaces related to defects. However, only vertical advancement was observed at pH 1 on this surface consistent with the observation of isolated islands on the surface during atomic force microscopy investigations after the experiment. Raman analysis of the precipitated phase showed that it was not one of the thermodynamically stable phases expected from PHREEQC modeling. However, the correlation between the siloxane ring peak of amorphous silica with a similar peak in the precipitate spectrum, in conjunction with previous experimental and natural observations, indicates that the precipitate was a Si-enriched amorphous phase. Therefore, precipitation can facilitate the further dissolution of olivine on this surface as long as it does not completely armor the surface. Precipitate formation on surfaces associated

with outcropping defects supports the natural observations of preferential dissolution and serpentinization along these defects implying that the fast dissolution of these surfaces will play a critical role during olivine replacement. In addition, comparison with flow-through experiments indicates that outflow fluid chemistry may provide an incomplete picture of processes occurring during olivine dissolution.

Keywords: Interferometry, dissolution, precipitation, olivine

1. Introduction

Olivine has recently been recognized as a key mineral for many environmental remediation schemes such as acid mine drainage (Kleiv and Thornhill, 2008), CO_2 (Jarvis et al., 2009) and sulfur sequestration (Rappold and Lackner, 2010). In addition, the natural reaction of olivine with fluids plays an important role in acidic fluid neutralization (Varekamp et al., 2009) and its reaction with seawater to produce serpentine minerals has important consequences for the rheology and geochemistry of the oceanic lithosphere (Escartin et al., 1997, Bach and Früh-Green, 2010). Although extensive research has been conducted into olivine reactivity most olivine dissolution experiments are limited to flow-through experiments that use ground olivine (e.g., Oelkers, 2001; Pokrovsky and Schott, 2000). However, there is evidence that in nature olivine dissolution occurs preferentially along specific crystallographic planes. For example, olivine that has undergone mantle flow has an anisotropy that causes parting along specific directions enabling the (010) surface to become accessible to fluids (Boudier et al., 2010). In experiments, dissolution of ground olivine also produces surface features that are attributed to preferential dissolution at dislocations and different cleavage planes (Grandstaff, 1978). Awad et al. (2000) studied dissolution at the (010), (100) and (001) surfaces of olivine and showed that

preferential dissolution occurred at the (010) surface. However, the experiments of Awad et al. (2000) were conducted by cutting and mechanically polishing an orientated olivine crystal and measuring the crystal size periodically to determine the dissolution rate. Previous work on calcite dissolution indicates that this method of sample preparation can increase the dissolution rate due to the formation of defects associated with mechanical grinding (Macinnis and Brantley, 1992).

To explore the dependence of crystallographic orientation on olivine dissolution we have performed in-situ measurements using phase-shift interferometry (PSI) experiments on three distinct olivine surfaces. The results of this study advances our understanding of preferential olivine dissolution as well as the concomitant precipitation of new phases that also occurred during our experiments and have been observed in nature (Boudier et al., 2010) and previous experimental investigations (Davis et al., 2009; King et al., 2010).

2. Methods

Naturally well-defined faces of gem quality euhedral forsteritic olivine crystals from the Sapat Complex, Kohistan, Pakistan were used as the starting material (Fig. 1). Samples of the surfaces were sliced along the crystal faces by sticking the surface face-down onto a glass slide and cutting it into 3 x 3 x 1 mm microchips. The glass slide and glue were then removed using acetone. Although the faces are macroscopically well defined, the surfaces had a roughness that was too high for direct use in PSI experiments. Thus, we chemically smoothed the surfaces prior to the experiment using the ‘spinning method’ in which the crystal is spun in 0.12 M HF solution at 20 °C until portions of the surface were flat enough to produce clear interference fringes on the PSI. Using HF acid spinning also cleaned the surface of any trace of the fibrous serpentine minerals that are associated phases with olivine crystals from the Sapat region (Bouilhol et al.,

2012). This treatment should prevent the formation of a Si-enriched layer on the olivine surface, as proposed by Pokrovsky and Schott (2000), because the Si can also be removed as soluble silicon fluorides. The spinning time needed to achieve the required degree of smoothness was dependent on the initial surface roughness but was typically a few minutes. The HF solution was renewed every second minute to prevent the saturation of silica. After smoothing, the surfaces were ultrasonically cleaned in deionized water. Due to the formation of large etch pits after smoothing, the crystallographic orientation of the individual surfaces could not be easily measured. Therefore, the original crystallographic orientation of the crystal face, shown for a typical crystal in Figure 1, was taken as the surface present.

A 0.1 M NaCl solution was prepared from solid reagents dissolved in deionized water. This solution was then placed in a sealed container and heated in an oven at 40 ºC overnight to reduce the concentration of dissolved gases. To obtain solutions with a range of pHs 0.1 M HCl was carefully added to this solution.

Phase-shift interferometry provides nanoscale resolved measurements of ultra-slow growth and dissolution of minerals (e.g., van Driessche et al., 2011) with a detection limit of $<10^{-5}$ nm/sec, depending on the stability of the machine, light wavelength and refractive index of the solution or mineral (e.g., Ueta et al., 2013). This technique has the benefit of a larger lateral area of study than that of other in-situ experimental methods such as atomic force microscopy (AFM) and can be used to obtain long-term measurements of dissolution and growth (see e.g. Green and Lüttge, 2006). The olivine dissolution measurements were conducted on the Fabulous phase-shift interferometer built in-house at Tohoku University, which uses modified Linnik-type interference optics and a white light source. A detailed description of the technique can be found in the appendix and Satoh et al. (2007). To set up the experiments samples were first attached to the

sample mount using silicone glue and gold particles deposited on the surface. The sample mount was then secured into the sample cell, which was subsequently closed. The sample cell was flushed with deionized water to wash the surface before the experiment and to remove any unstable gold particles. During flushing, bubbles were removed by gently tapping the sample cell. The sample cell was held at 22 °C ±0.2 °C (the temperature of the clean-room). The fluid was pumped through the cell using a syringe pump with a flow rate of 40 μL/min resulting in a linear velocity of 15 μm/sec at the dissolving surface. Each surface was reacted with the 0.1 M NaCl solution (pH 5.9) followed by pH 4, 3, 2 and 1 solutions. The reactant solutions were run through the reaction cell for at least 10 minutes prior to the beginning of the experiment to purge the cell of the previous solution. When all experiments on a surface had been completed the sample cell was flushed with ethanol and immediately opened to prevent further reaction of the olivine with the solution. After each experiment the whole fluid cell was cleaned in an ultrasonic bath using a dilute HCl solution followed by deionized water and air dried.

Changes in surface roughness were used to provide additional information about the dissolution and growth occurring at the different olivine surfaces. Surface roughness was examined for areas of the surface (30 x 33 pixels, 9.0 x 9.9 μm) surrounding each of the points analyzed for vertical velocity. Two parameters, *Ra* and *Rz*, were calculated for the roughness following the procedure of Fischer and Lüttge (2007). *Ra* is a measure of the overall surface roughness and was calculated by separating each of the areas into lines, taking the standard deviation of the grayscale intensity for each line separately and then calculating the arithmetic mean of the standard deviation of all the lines within the individual areas on the surface. The change in *Ra* during the experiment was then calculated as $\Delta Ra = Ra_{end} - Ra_{beg}$.

The second roughness parameter *Rz* determines the deviation of the five highest (z_{pi}) and five lowest (z_{vi}) grayscale values from the mean grayscale for a designated area and can provide

information about how individual mineral surface areas are dissolving and thus changing in roughness. For example, a negative value of *Rz* indicates that the surface area had a few points with a very low height or grayscale value however the mean grayscale value was similar to the majority of points used in the calculation i.e., there were specific, isolated lower points in the area examined. A positive value of *Rz* suggests that the surface was comprised of high islands whilst the average grayscale for the surface and thus majority of the surface area was comparatively low. The Rz parameter was calculated using

$$R_z = \frac{\sum_{i=1}^{5}(z_{pi} - \mu) + \sum_{i=1}^{5}(z_{vi} - \mu)}{5}$$

where the average (μ) was calculated using

$$\mu = \frac{1}{MN}\sum_{k=0}^{M-1}\sum_{l=0}^{N-1} z(x_k y_l) \ .$$

The difference in *Rz* roughness between the beginning and the end of the experiment (ΔRz) for each area was taken using the same procedure used to determine ΔRa.

The (021) surface was also examined using a Digital Instruments Nanoscope III Multimode atomic force microscope (AFM) (Digital Instruments, Bruker) because AFM has a better x-y resolution than PSI. The AFM was equipped with a Si_3N_4 tip (Veeco Instruments tip model NP-S20) with spring constants 0.12 N/m and 0.58 N/m. Images were taken in contact mode and analyzed using the Nanoscope software (Version 5.31r1).

Raman spectroscopy was used to try to identify the precipitated phase. Raman spectra were collected with a high-resolution Jobin Yvon HR800 Raman spectrometer using the 532 nm line of a 14 mW Nd-YAG laser calibrated using the 520.7 cm^{-1} band of silicon. After passing through a 100 μm entrance slit the scattered Raman light was dispersed by a grating of 1800 grooves/mm. A hole size of 100 μm was used to limit the penetration depth of the laser into the sample. The

Raman spectra from the sample were compared to RRUFF project (Downs, 2006) reference spectra of the most thermodynamically stable phases calculated using the geochemical modeling program PHREEQC (Parkhurst and Appelo, 2000). The simulations were conducted with different surface areas beginning with a 3 mm x 3 mm flat surface. The effect of different fluid-solid ratios was also examined because the exact amount of solution between the glass window of the PSI sample cell and the crystal was unknown. The Lawrence Livermore National Laboratory database was used in the simulations.

3. Results

Dissolution was observed on all surfaces during the experiments and was accompanied by the formation of etch pits comparable in shape to those observed during natural weathering by Velbel (2009). The average vertical retreat velocities for each surface can be found in Table 1 and a plot of the different rates of surface retreat in Figure 2. Step retreat velocity shows a strong correlation with the solution acidity where the rate of step retreat increased with decreasing solution pH (Fig. 2c).

3.1 Crystal faces

The (010) surface had large flat areas with striations before the HF treatment. According to Jan and Khan (1996) the striations are parallel to the c-axis [001] direction. During a smoothing test extensive dissolution of the (010) surface produced square etch pits that were aligned with the striations already present on the surface. The shape of the etch pits and their alignment to form channels was consistent with those observed by Kirby and Wegner (1978) on a cut and polished (010) surface.

During the dissolution experiments minimal change in the surface features was observed. Dissolution at the (010) surface showed a gradual increase in the rate of normal surface retreat as the pH was lowered. Indications of rising surface height were observed in the pH 1 experiment, however, it was followed by a period of dissolution and thus was attributed to an instability of the gold surface during the first part of the experiment. Only olivine peaks were observed in the Raman spectrum, thus no new phases were detected within the uncertainties of the measurements. The area studied on the (110) surface consisted of smooth areas of surface that had smaller rougher areas between them. Similarly to the (010) surface, the (110) surface morphology did not change dramatically during the experiment. Reaction of the (110) surface was conducted at pH 1 and pH 6 only for comparison to the rates from the (010) surface. Increase in the surface height was found for all points on this surface at pH 6, however only retreat of the surface was observed in the pH 1 solution. The retreat determined for the pH 1 solution was faster than observed for the (010) surface with the same solution. As for the (010) surface, no precipitation was observed on the (110) surface after the experiments.

3.2 Defect-related surface

The (021) surface was examined prior to the experiments using AFM due to the presence of some unexpected surface features. The AFM images of the starting surface show that the studied area of this surface is composed of terraces (Fig. 3a) with the step faces consisting of etch hillocks (also known as mammillary structures) similar to those observed in natural weathering (Velbel, 1993) and during olivine dissolution in experiments (Grandstaff, 1978; King et al. 2010). The steps have an average height of 90 nm and the etch hillocks along the step face have a maximum width of 120 nm. Some of the smaller steps were only 45 nm in height. During

dissolution and growth the stepped structures became less prominent (Fig. 3b), except at the etch pit walls.

Vertical retreat rate of the (021) surface increased with increasing acidity until experiments at pH 1 and 2 where all points showed an increase in the height of the surface. Specific spots on the surface also showed an increase in height at lower acidities, pH 4 and 6, however only surface retreat was observed in the experiment at pH 3. To determine whether the formation of a new phase was the cause of the height increase, the surface was also examined using AFM after the experiments (Fig. 3b). The AFM image confirmed the presence of a new phase on the surface that consisted of rounded islands with one slightly elongated axis. Small islands covered the entire surface and had a maximum width of 0.3 μm. The average height of the new phase was 14 nm, however the AFM image shows evidence that further nucleation and growth occurred on top of existing islands forming stacks up to 50 nm high. In some areas large particles of up to 1 μm height were also observed.

We attempted to characterize the newly formed islands using Raman spectroscopy on the (021) sample (Fig. 4). Small, broad bands at 489 and 709 cm^{-1} that were not found in the reference olivine spectrum can be attributed to the precipitated phase. To help identify the precipitated phase the reaction was simulated using the geochemical modeling program PHREEQC assuming a system with no flow. This enabled us to predict the most thermodynamically stable phases expected under experimental conditions where growth was observed. In the 0.1 M NaCl solution (pH 6) the simulations showed that when a surface area of 0.3 cm^2 or greater was present the system was supersaturated with respect to hematite and talc. In contrast, at pH 1 the fluid is predicted to be supersaturated with respect to amorphous silica and talc (and obviously also with respect to other more stable crystalline silica phases that are unlikely to crystallize at 22 °C). Therefore, talc and amorphous silica were taken as reference phases to compare with the Raman

spectrum of the phase precipitated in the pH 1 experiments along with the phase sepiolite, which has been observed to form in low temperature experiments where talc or serpentine are expected to be thermodynamically stable (Wollast et al., 1968). Of the peaks associated with the precipitate only the peak at 489 cm^{-1} had a similar peak in the reference spectra for the most stable phases predicted by thermodynamic calculations. This peak is comparable to the broad peak in the amorphous silica spectrum that is assigned to 4-membered siloxane ring structures (Sharma et al., 1981).

3.3 Roughness analysis

The results of the roughness analysis are shown in Figure 5. During the reaction of the surface with low acidity solutions the different areas of the surface exhibit minimal scatter of ΔRa (Fig. 5a). This scatter in ΔRa increased for the individual areas for experiments with solutions of increasing acidity. Each surface showed an equal number of areas that had increased and decreased in *Ra*, with the exception of the pH 3 experiment conducted with the defective (021) surface, which displayed a large increase of *Ra* for the majority of the surface areas examined.

The change in *Rz* is more complicated to interpret than variations in *Ra* because the calculated *Rz* values can have either a positive or negative value depending on the grayscale distribution. As observed for the *Ra* parameter, the different areas on the surface exhibited different behavior with respect to the *Rz* value. In all experiments, with the exception of the defective (021) surface reacted with a pH 6 solution, there were areas that exhibited both an increase and decrease in *Rz*. Some areas also changed from positive to negative values of *Rz*. For ΔRz the scatter of points for each area showed a similar change to that measured using Ra (Fig. 5b). A few outlying points are the exception to this observation, and showed a large decrease in ΔRz during the pH 1 experiment on the (010) crystal face and a large increase in ΔRz for one area in the pH 3 experiment for the

defective (021) surface. These points also correlate to some of the lowest and highest Δ*Ra* values observed in the experiments (Fig. 5c). As can be seen from Fig. 5c, there was no systematic relationship between an increase or decrease in Δ*Ra* value in comparison to the Δ*Rz* value for each area.

4. Discussion

4.1 Dissolution rates

Comparison of the surfaces showed that the surface reactivities follow the order defective (021) > crystal face (110) > crystal face (010) thus each surface exhibited a different reactivity. As temperature, pressure and flow rate were kept constant it can be inferred that this difference was dependent on the original surface structure. Typically, the different reactivities of surfaces are described using concepts such as the periodic bond chain (PBC) theory of Hartman and Perdok (1955a, 1955b, 1955c). In this model the different surfaces on a crystal can be separated into three different classes, F faces (flat faces), S faces (stepped faces) and K faces (kinked faces). The faces are determined by the number of periodic chains of strong bonds (PBCs) within the olivine structure along a specific direction that are associated with different surfaces. A K face has no PCBs associated with it whereas an S face has only one PCB and an F face contains PCBs in at least two different directions. These different classes of surface exhibit different reactivities often with increasing reactivity in the order K > S > F. For olivine the majority of the crystal faces observed on natural crystals are denoted as F faces, including the three faces that we have studied ('t Hart, 1978). Therefore, the different surfaces should have similar stabilities. Recent computational work by de Leeuw et al. (2000) shows that the stabilities and thus the reactivity of the studied surfaces do not vary greatly when the surfaces are hydrated. Therefore, the high reactivity observed for the (021) surface, particularly with solutions of pH 3 or lower, cannot be

257 adequately explained by the crystal face reactivity alone indicating that the high reactivity was
258 related to the terraces present on this surface.

259 Etch hillocks are attributed to preferential dissolution along specific crystal planes and
260 dislocations (Grandstaff, 1978). Thus the formation of etch hillocks at the step edges (Fig. 3a) on
261 the (021) surface indicates that the terraces present were uncovered due to preferential dissolution
262 along defects rather than normal surface retreat. Godinho et al. (2012) demonstrated that CaF_2
263 surfaces with a high step density have increased dissolution rates in comparison to flat surfaces
264 and therefore the vertical velocity measurements were normalized to the step density (see
265 Appendix). Comparison of the step retreat velocity (Fig. 2c) shows that at pH 4 and 6 the defect-
266 related terrace areas have a similar retreat rate to that observed on the (010) surface. However, at
267 pH 3 the rate of step retreat increased and was higher than that of the (010) surface, consistent
268 with the formation of precipitates on this surface at pH 2 and 1 due to the fast dissolution of the
269 defect related features. The relationship between the step density and the retreat rate as step
270 retreat velocity, also shows that the observed reactivity difference from the vertical retreat rates
271 can be attributed to the step, kink and dislocation density at the different surfaces.
272 Dissolution at acidic pHs for the (110) and (010) crystal face surfaces shows much more limited
273 dissolution than observed on the (021) surface. The increased reactivity of the (110) surface was
274 expected from PCB theory, which indicates that the (010) surface is more stable than the (110)
275 surface ('t Hart, 1978). However, the dissolution rates of the (010) and (110) surfaces remained
276 similar, as expected from considerations of the hydroxylated surface stabilities of 0.26 and 0.27
277 J/m^2 for the (110) and (010) surface respectively calculated by de Leeuw et al. (2000).
278 In pH 4 and 6 solutions the normal surface retreat determined in situ was faster than those
279 calculated for ground olivine in flow-through experiments (Pokrovsky and Schott, 2000) (Table
280 2, Fig. 6). The evidence for growth at pH 6 on the (110) and (021) surfaces and the expected

281 removal of only a few nms of material based on the measured dissolution rates, results in silica
282 layers similar in size to those previously observed on olivine (Hellmann et al. 2012), and
283 indicates that a relative rate could have been measured during the course of the experiments. If
284 this is the case, the real dissolution rates could be even faster. In contrast, dissolution at the (110)
285 and (010) crystal face surfaces examined in this study showed a similar dissolution rate at more
286 acidic pHs to those reported for flow-through experiments. This suggests that at higher pH, where
287 the dissolution of olivine is slower, anisotropy between the different surfaces plays a role in the
288 overall dissolution, whereas in low pH solutions where olivine dissolution is faster the effect of
289 anisotropic dissolution is not as important.
290
291 4.2 Surface reactivity
292 Recent in depth analysis of surface reactivity by Fischer et al. (2012) has demonstrated the
293 importance of reactivity distribution across a surface. The PSI pixel data samples a small area of
294 the surface (0.09 μm^2) and was limited to the terrace areas as the etch pits did not produce
295 reliable results, however, examination of the change in terrace area roughness can still provide
296 interesting insights into the changes of the surface during the experiments. The roughness
297 parameters calculated for the sample points also showed that on all of the surfaces each area
298 examined exhibited a unique behavior, however the overall behavior of the different surfaces is
299 similar under similar conditions, even between the defective (021) surface and the crystal faces.
300 For example, there is a similar scatter in dissolution rate in pH 6 experiments for both the
301 defective (021) surface and the planar (010) surface but *Ra* and *Rz* changed only minimally (Fig.
302 5). At pH 1 there is a similar variation in the retreat rates on both the (110) and (010) crystal faces
303 to that observed at pH 6 but there is a larger difference in the change in surface roughness at the
304 individual surface points. In addition, the change in roughness does not directly reflect the

reactivity of the surface measured by retreat rate as demonstrated by the relationship between rate and Ra during the pH 3 experiments on the (021) surface (insert in Fig. 5a). The change in roughness for each area also shows no correlation with the surface slope (Fig. 7) and therefore suggests that the change in roughness of individual areas was not controlled by the higher roughness associated with higher step density.

Similarly to the *Ra* roughness parameter, *Rz* also gives an indication of the homogeneity of the olivine surface dissolution, however this parameter can also provide an insight into how the individual areas on the surface dissolve. The largest changes in the *Rz* value are observed for the pH where the fastest dissolution rate was observed. This correlates with the large increase in roughness that was observed for the fastest dissolution rates with the ΔRa parameter. However, although the *Rz* parameter shows that as the solution acidity increased the different surface areas exhibited different behavior no systematic decrease or increase in *Rz* was observed in relation to the initial surface area morphology. The observation that individual areas can react differently and non-systematically during each experiment highlights the importance of examining many different spots during the in-situ analysis of olivine dissolution. In particular, it highlights the importance of examining the 'rate spectra' for a surface, as described by Fischer et al. (2012), to establish a thorough understanding of how a surface dissolves. However, the importance of these rate spectra also needs to be examined at different conditions, as the olivine PSI experiments indicate that although changes in roughness may vary dramatically across surface areas with very similar characteristics, i.e., a terrace rather than a step area, the impact on the actual reactivity, reflected in the dissolution rate, does not necessarily mirror this change in roughness.

4.3 Precipitation

Increasing surface height during the PSI experiments is related to the growth of new phases at the surface. From the experimental results two different growth events can be determined. The first growth was observed during reactions with the pH 4 and 6 solutions and the second with the pH 1 and 2 solutions. The first growth event at low acidity is expected to be limited, as only a few points on the (021) surfaces exhibited growth. The further dissolution of the surface at all points examined on the (021) surface and the similarities of the dissolution rates for each point on the surface indicates that the new phase was metastable and redissolved or stopped growing, thus at pH 3, only dissolution of the olivine was detected. For the (110) surface the purging of low acidity solution before measuring the reaction with a high acidity solution was also expected to have cleared the surface of any precipitated phases. The second growth event, observed on the (021) surface terraces at high acidity, was more stable and resulted in the formation of islands of a new phase on the surface. Growth was the dominant process on the defect-related (021) surface at low pH because dissolution was not detected at any point analyzed on the surface during the experiments at pH 1 and 2.

Olivine dissolution has been proposed to occur via the exchange of Mg for H^+ (protonation) from the solution at the surface creating isolated silica tetrahedra that condense to form an amorphous silica-rich layer (Pokrovsky and Schott, 2000). Computer simulations by Liu et al. (2006) supported this hypothesis and showed that removal of the Si into solution is the rate determining step of olivine dissolution. However, Zakaznova-Herzog et al. (2008) found no evidence for the development of a Si-enriched leached layer. In our experiments the formation of islands of a new phase and the increased height of the surface during the experiment indicates that precipitation occurred rather than condensation of the silica tetrahedra that remain attached to the olivine surface, which should show negligible height difference. The formation of similar precipitates has been documented in many different silicate systems including wollastonite (Daval et al.,

2009; Ruiz-Agudo et al., 2012), diopside (Daval et al., 2013) and olivine at high acid concentrations (King et al., 2011). These studies show consistent evidence for an interface-coupled dissolution precipitation mechanism (Putnis and Putnis, 2007) for mineral replacement where the dissolving mineral phase progressively increases the interfacial fluid saturation until a critical supersaturation is reached and a new phase is precipitated. Further dissolution is facilitated in this mechanism by the depletion of ions in the interfacial solution due to the growth of the new phase. The continued vertical advancement of the surface and nucleation of new islands suggests that the olivine surface continues to dissolve as the precipitate grows but that due to the large distribution of the precipitates across the surface this could not be sampled independently by the 0.3 μm pixel size.

PHREEQC calculations showed that the most stable phases expected to form in the reaction of olivine with saline fluids at pH 1 and 2 are talc and amorphous silica, of which amorphous silica had the highest supersaturation. Comparison of the Raman peaks assigned to the precipitated phase with reference spectra for the theoretically stable phases revealed that the broad peak in the amorphous silica spectrum that represents siloxane ring structures corresponded to the precipitated phase peak at 489 cm^{-1}. Specifically, the sharper peak in the sample spectrum implies that most of the siloxane ring structures are small 4-membered rings. However, the precipitated phase also had a peak at 709 cm^{-1} that is not present in the amorphous silica spectrum, but is in an area of the spectrum where intense peaks attributed to intra-tetrahedral linkages e.g., Si-O stretching modes of bridging O atoms, within the silicate structure are found (Blaha and Rosasco, 1978; Huang et al., 2000; Kloprogge et al., 1999; McMillan, 1984). Hydrated amorphous Mg-silicate phases are observed in nature (Rumori et al., 2004) and experiments (King et al., 2010) as precursors to crystalline phases during olivine replacement. Therefore, in conjunction with nuclear magnetic resonance studies, which have shown that the amorphous phase has a

376 composition similar to that of serpentine ($Mg_2Si_3O_5(OH)_4$) (Davis et al., 2009), we expect that the
377 precipitated phase is a hydrated amorphous Mg-silicate phase probably with additional Fe due to
378 the presence of Fe in Sapat olivine, as observed at higher temperature by Saldi et al. (2013) and
379 King et al. (2010). The precipitation of an amorphous phase indicates that the interfacial fluid
380 must have been highly supersaturated because amorphous phases are more soluble than their
381 crystalline counterparts.
382
383 5. Implications
384 The different reactivities observed on the olivine surfaces have important implications for
385 dissolution in the natural environment. Step retreat velocities imply that the terraces related to
386 defects present at the (021) surface dissolved at a similar rate to the (010) and (110) surfaces,
387 however, the outcropping of these defects at the (021) surface increased its reactivity. The fast
388 dissolution at the surface with etch hillocks also caused the precipitation of a Mg-silica phase in
389 solutions with a pH of 2 or 1. The overall effect of these precipitates on olivine dissolution is
390 difficult to quantify because further dissolution will depend on whether the precipitate completely
391 armors the surface. Precipitating phases that remove olivine constituent ions from solution can
392 aid olivine dissolution by increasing the undersaturation of the interfacial solution with respect to
393 olivine. However, the further dissolution of olivine will also be dependent on diffusion through
394 the precipitated layer as the reaction is controlled by the interfacial solution chemistry.
395 Densification of amorphous silica precipitates and therefore reduction in porosity is expected to
396 occur with time as the silica units condense or polymerize (Cailleteau et al., 2008), which would
397 slow dissolution and passivate the reaction, especially if Fe(III) is present (Saldi et al., 2013). In
398 contrast, the formation of columnar serpentine from the amorphous phase can provide fluid
399 pathways for the infiltrating fluid (Boudier et al., 2010) and is expected to create fracturing due to

volume expansion (Plümper et al., 2012a; Rudge et al., 2010). In olivine percolation experiments solution flow rate has been shown to play an important role in the location of precipitation during fluid infiltration (Andreani et al., 2009) with different phases precipitating in different flow zones. Thus, future investigations should focus on the nucleation rate and the effect of different temperatures and pressures on the phase precipitated to help clarify the effect of precipitation during olivine dissolution.

The similarity between the dissolution rates determined at pH 3 and lower by Pokrovsky and Schott (2000) using outlet fluid chemistry and this in-situ study indicates that the outlet fluid chemistry of ground olivine experiments is controlled by the dissolution of surfaces similar to the (110) and (010). This further implies that the effect of the faster dissolving surfaces associated with outcropping defects cannot be observed from outlet solution concentrations due to the concomitant formation of the amorphous Mg-silicate precipitates. These precipitates are limited to specific surfaces at low pH and are below the imaging capability of methods such as scanning electron microscopy that are typically used to examine surfaces after experiments. Thus, experiments based on outflow fluid chemistry alone may provide an incomplete picture of processes occurring during olivine dissolution. The in situ study also shows that olivine reactivity with respect to dissolution can vary from one crystallographic surface to another as well as in different parts of the same surface with similar characteristics, such as terraces. Finally, the observation of precipitate formation on surfaces associated with outcropping defects supports the natural observations of preferential serpentinization along these defects (Plümper et al. 2012b) implying that it will be the reactivity of these surfaces that will control olivine reactivity in nature. A recent discussion of the general implications of variable dissolution rates of different crystal surfaces and their evolution with time, to conventional flow-through dissolution experiments on powders can be found in Lüttge et al. (2013).

Acknowledgments

The majority of this work was funded by two Global COE student internships awarded to Dr. H.E. King for two month long stays in Prof. Tsukamoto's laboratory at the Department of Earth and Planetary Science, Tohoku University to work on the PSI. Additional funding was provided by the European Early Stage Training Network MIN-GRO contract number MRTN-CT-2006-035488 and the DFG grant PU153/16-1 awarded to Prof. Andrew Putnis. The authors would like to thank Dr. M. Menneken for assistance with the Raman spectroscopy performed at the Institut für Anorganische und Analytische Chemie, University of Münster and Dr. E. Ruiz-Agudo for assistance with the AFM at the Institut für Mineralogie, University of Münster. We also thank one anonymous reviewer and Dr. Damien Daval for their constructive comments that helped to improve the manuscript during the review process.

References Cited

't Hart, J. (1978) The structural morphology of olivine; I. A qualitative derivation. Canadian Mineralogist, 16, 175-186.

Andreani, M., Luquot, L., Gouze, P., Godard, M., Hoise, E., and Gibert, B. (2009) Experimental study of carbon sequestration reactions controlled by the percolation of CO_2-rich brine through peridotites. Environmental Science and Technology, 43, 1226-1231.

Awad, A., van Groos, A.F.K., and Guggenheim, S. (2000) Forsteritic olivine: Effect of crystallographic direction on dissolution kinetics. Geochimica et Cosmochimica Acta, 64, 1765-1772.

446 Bach, W., Früh-Green, G.L. (2010) Alteration of the oceanic lithosphere and implications for
447 seafloor processes. Elements, 6, 173-178.
448 Blaha, J.J., and Rosasco, G.J. (1978) Raman microprobe spectra of individual microcrystals and
449 fibers of talc, tremolite, and related silicate minerals. Analytical Chemistry, 50, 892-896.
450 Boudier, F., Baronnet, A., and Mainprice, D. (2010) Serpentine mineral replacements of natural
451 olivine and their seismic implications: Oceanic lizardite versus subduction-related
452 antigorite. Journal of Petrology, 51, 495-512.
453 Bouilhol, P., Burg, J.-P., Bodinier, J.-L., Schmidt, M.W., Bernasconi, S. M. and Dawood, H.
454 (2012) Gem olivine and calcite mineralization precipitated from subduction-derived fluids
455 in the Kohistan arc-mantle (Pakistan). The Canadian Mineralogist, 50, 1291-1304.
456 Cailleteau, C., Angeli, F., Devreux, F., Gin, S., Jestin, J., Jollivet, P., and Spalla, O. (2008)
457 Insight into silicate-glass corrosion mechanisms. Nature Materials, 7, 978-983.
458 Daval, D., Hellmann, R., Saldi, G.D., Wirth, R., and Knauss, K.G. (2013) Linking nm-scale
459 measurements of the anisotropy of silicate surface reactivity to macroscopic dissolution
460 rate laws: New insights based on diopside. Geochimica et Cosmochimica Acta, 107, 121-
461 134.
462 Daval, D., Martinez, I., Guigner, J.M., Hellmann, R., Corvisier, J., Findling, N., Dominici, C.,
463 Goffe, B., and Guyot, F. (2009) Mechanism of wollastonite carbonation deduced from
464 micro- to nanometer length scale observations. American Mineralogist, 94, 1707-1726.
465 Davis, M.C., Brouwer, W.J., Wesolowski, D.J., Anovitz, L.M., Lipton, A.S., and Mueller, K.T.
466 (2009) Magnesium silicate dissolution investigated by ^{29}Si MAS, ^{1}H-^{29}Si CPMAS, ^{25}Mg
467 QCPMG, and ^{1}H-^{25}Mg CP QCPMG NMR. Physical Chemistry Chemical Physics, 11,
468 7013-7021.

de Leeuw, N.H., Parker, S.C., Catlow, C.R.A., and Price, G.D. (2000) Modelling the effect of water on the surface structure and stability of forsterite. Physics and Chemistry of Minerals, 27, 332-341.

Deer, W.A., Howie, R.A., and Zussman, J. (1992) An Introduction to the Rock-Forming Minerals. Longman Scientific and Technical, London, U.K.

Downs, R.T. (2006) The RRUFF Project: An intergrated study of the chemistry, crystallography, Raman and infrared spectroscopy of minerals. Program and abstracts of the 19th General Meeting of the International Mineralogical Association in Kobe, Japan, O03-13.

Escartin, J., Hirth, G., and Evans, B. (1997) Effects of serpentinization on the lithospheric strength and the style of normal faulting at slow-spreading ridges. Earth and Planetary Science Letters, 151, 181-189.

Fischer, C., Arvidson, R.S., and Lüttge, A. (2012) How predictable are dissolution rates of crystalline material? Geochimica et Cosmochimica Acta, 98, 177-185.

Fischer, C., and Lüttge, A. (2007) Converged surface roughness parameters - A new tool to quantify rock surface morphology and reactivity alteration. American Journal of Science, 307, 955-973.

Godinho, J.R.A., Piazolo, S. and Evins, L.Z. (2012) Effect of surface orientation on dissolution rates and topography of CaF_2. Geochimica et Cosmochimica Acta, 86, 392-402.

Grandstaff, D.E. (1978) Changes in surface area and morphology and the mechanism of forsterite dissolution. Geochimica et Cosmochimica Acta, 42, 1899-1901.

Green, E., and Lüttge, A. (2006) Incongruent dissolution of wollastonite measured using vertical scanning interferometry. American Mineralogist, 91, 430-434.

Hartman, P., and Perdok, W.G. (1955a) On the relations between structure and morphology of crystals. I. Acta Crystallographica, 8, 49-52.

- (1955b) On the relations between structure and morphology of crystals. II. Acta Crystallographica, 8, 521-524.

- (1955c) On the relations between structure and morphology of crystals. III. Acta Crystallographica, 8, 525-529.

Hellmann, R., Wirth, R., Daval, D., Barnes, J.-P., Penisson, J.-M., Tisserand, D., Epicier, T., Florin, B., and Hervig, R.L. (2012) Unifying natural and laboratory chemical weathering with interfacial dissolution-reprecipitation: A study based on the nanometer-scale chemistry of fluid-silicate interfaces. Chemical Geology, 294-295, 203-216.

Huang, E., Chen, C.H., Huang, T., Lin, E.H., and Xu, J.-A. (2000) Raman spectroscopic characteristics of Mg-Fe-Ca pyroxenes. American Mineralogist, 85, 473-479.

Jan, M.Q., and Khan, M.A. (1996) Petrology of gem peridot from Sapat mafic-ultramafic complex, Kohistan, NW Himalaya. Geological Bulletin of the University of Peshawar, 29, 17-26.

Jarvis, K., Carpenter, R.W., Windman, T., Kim, Y., Nunez, R., and Alawneh, F. (2009) Reaction mechanisms for enhancing mineral sequestration of CO_2. Environmental Science and Technology, 43, 6314-6319.

King, H.E., Plümper, O., Geisler, T., and Putnis, A. (2011) Experimental investigations into the silicification of olivine: Implications for the reaction mechanism and acid neutralization. American Mineralogist, 96, 1503-1511.

King, H.E., Plümper, O., and Putnis, A. (2010) Effect of secondary phase formation on the carbonation of olivine. Environmental Science and Technology, 44, 6503-6509.

Kirby, S.H., and Wegner, M.W. (1978) Dislocation substructure of mantle-derived olivine as revealed by selective chemical etching and transmission electron-microscopy. Physics and Chemistry of Minerals, 3, 309-330.

517 Kleiv, R.A., and Thornhill, M. (2008) Predicting the neutralisation of acid mine drainage in
518 anoxic olivine drains. Minerals Engineering, 21, 279-287.
519 Kloprogge, J.T., Frost, R.L., and Rintoul, L. (1999) Single crystal Raman microscopic study of
520 the asbestos mineral chrysotile. Physical Chemistry Chemical Physics, 1, 2559-2564.
521 Liu, Y., Olsen, A.A., and Rimstidt, J.D. (2006) Mechanism for the dissolution of olivine series
522 minerals in acidic solutions. American Mineralogist, 91, 455-458.
523 Lüttge, A., Arvidson, R.S. and Fischer, C. (2013) A stochastic treatment of crystal dissolution
524 kinetics. Elements, 9, 183-188.
525 Macinnis, I.N., and Brantley, S.L. (1992) The role of dislocations and surface morphology in
526 calcite dissolution. Geochimica et Cosmochimica Acta, 56, 1113-1126.
527 McMillan, P. (1984) Structural studies of silicate glasses and melts - Applications and limitations
528 of Raman spectroscopy. American Mineralogist, 69, 622-644.
529 Majano, G., Mintova, S., Ovsitser, O., Mihailova, B., and Bein, T. (2005) Zeolite Beta nanosized
530 assemblies. Microporous and Mesoporous Materials, 80, 227-235.
531 Oelkers, E.H. (2001) An experimental study of forsterite dissolution rates as a function of
532 temperature and aqueous Mg and Si concentrations. Chemical Geology, 175, 485-494.
533 Parkhurst, D.L., and Appelo, C.A.J. (1999) User's guide to PHREEQC (Version 2) - A computer
534 program for speciation, batch-reaction, one-dimensional transport, and inverse
535 geochemical calculations, Water-Resources Investigations Report 99-4259, Denver,
536 Colorado.
537 Plümper, O., Royne, A., Magraso, A., and Jamveit, B. (2012a) The interface-scale mechanism of
538 reaction-induced fracturing during serpentinization. Geology, 40, 1103-1106.
539

Plümper, O., King, H.E., Vollmer, C., Ramasse, Q., Jung, H., and Austrheim, H. (2012b) The legacy of crystal-plastic deformation in olivine: High-diffusivity pathways during serpentinization. Contributions to Mineralogy and Petrology, 163, 701-724.

Pokrovsky, O.S., and Schott, J. (2000) Kinetics and mechanism of forsterite dissolution at 25 °C and pH from 1 to 12. Geochimica et Cosmochimica Acta, 64, 3313-3325.

Putnis, A., and Putnis, C.V. (2007) The mechanism of reequilibration of solids in the presence of a fluid phase. Journal of Solid State Chemistry, 180, 1783-1786.

Rappold, T.A., and Lackner, K.S. (2010) Large scale disposal of waste sulfur: From sulfide fuels to sulfate sequestration. Energy, 35, 1368-1380.

Rudge, J.F., Kelemen, P.B., and Spiegelman, M. (2010) A simple model of reaction-induced cracking applied to serpentinization and carbonation of peridotite. Earth and Planetary Science Letters, 291, 215-227.

Ruiz-Agudo, E., Putnis, C.V., Rodriguez-Navarro, C., and Putnis, A. (2012) Mechanism of leached layer formation during chemical weathering of silicate minerals. Geology, 40, 947-950.

Rumori, C., Mellini, M., and Viti, C. (2004) Oriented, non-topotactic olivine -> serpentine replacement in mesh-textured, serpentinized peridotites. European Journal of Mineralogy, 16, 731-741.

Saldi, G.D., Daval, D., Morvan, G., and Knauss, K. (2013) The role of Fe and redox conditions on olivine carbonation rates: An experimental study of the rate limiting reactions at 90 and 150 °C in open and closed systems. Geochimica et Cosmochimica Acta, 118, 157-183.

562 Satoh, H., Nishimura, Y., Tsukamoto, K., Ueda, A., Kato, K., and Ueta, S. (2007) In-situ
563 measurement of dissolution of anorthite in Na-Cl-OH solutions at 22 °C using phase-shift
564 interferometry. American Mineralogist, 92, 503-509.
565 Sharma, S.K., Mammone, J.F., and Nicol, M.F. (1981) Raman investigation of ring
566 configurations in vitreous silica. Nature, 292, 140-141.
567 Ueta, S., Satoh, H., Kato, H., Ueda, A. and Tsukamoto, K. (2013) A novel technique of in situ
568 phase-shift interferometry applied for faint dissolution of bulky montmorillonite in
569 alkaline solution. Journal of Nuclear Science and Technology, 50, 731-741.
570 van Driessche, A.E.S., Garcia-Ruiz, J.M., Tsukamoto, K., Patino-Lopez, L.D., and Satoh, H.
571 (2011) Ultraslow growth rates of giant gypsum crystals. Proceedings of the National
572 Academy of Sciences of the United States of America, 108, 15721-15726.
573 Varekamp, J.C., Ouimette, A.P., Herman, S.W., Flynn, K.S., Bermudez, A., and Delpino, D.
574 (2009) Naturally acid waters from Copahue volcano, Argentina. Applied Geochemistry,
575 24, 208-220.
576 Velbel, M.A. (1993) Formation of protective surface layers during silicate-mineral weathering
577 under well-leached, oxidizing conditions. American Mineralogist, 78, 405-414.
578 - (2009) Dissolution of olivine during natural weathering. Geochimica et Cosmochimica Acta,
579 73, 6098-6113.
580 Wollast, R., Mackenzie, F.T., and Bricker, O.P. (1968) Experimental precipitation and genesis of
581 sepiolite at earth-surface conditions. American Mineralogist, 53, 1645-1662.
582 Zakaznova-Herzog, V.P., Nesbitt, H.W., Bancroft, G.M., and Tse, J.S. (2008) Characterization of
583 leached layers on olivine and pyroxenes using high-resolution XPS and density functional
584 calculations. Geochimica et Cosmochimica Acta, 72, 69-86.

585

586 **Figure captions**

587 Figure 1. (a) Crystal structure from Deer et al. (1992) and (b) typical peridot crystal used in
588 experiments.

589 Figure 2. Plots of the vertical retreat velocity (a) and vertical advancement velocity (b) of the
590 different surfaces during the experiments with respect to the pH value of the solution. (c) Step
591 retreat calculated for the experiments vs. solution pH.

592 Figure 3. (a) AFM image of an area on the (021) surface with terraces before experiment. (b)
593 (021) surface after experiment.

594 Figure 4. Raman spectra of the (021) sample (black), reference olivine sample from Kohistan
595 (red) and possible precipitated phases. All reference spectra are from the RRUFF project (Downs,
596 2006) with the exception of amorphous silica, which is from Majano et al. (2005). Peaks in the
597 sample spectrum assigned to the precipitated phase are highlighted by boxes. The spectra show
598 only the first 800 cm^{-1} of the spectra due to the swamping of the sample and olivine spectra by
599 the intense bands above 800 cm^{-1}.

600 Figure 5. (a) Plot of ΔRa values against the dissolution rates determined for each of the points.
601 Insert shows the rates of the pH 3 experiment against ΔRa on a linear scale. (b) Dissolution rates
602 plotted in relation to ΔRz, (c) Comparison of the change in *Ra* and *Rz* during the experiment.

603 Figure 6. Comparison between dissolution rates of olivine surfaces with those of Pokrovsky and
604 Schott (2000) for ground olivine powder.

605 Figure 7. Plots showing the relationship between the slope, thus step density, in each area on the
606 surface and the corresponding area's ΔRa roughness parameter (a) or ΔRz roughness parameter
607 (b).

608

609

Tables

Table 1. Dissolution rates determined from the PSI experiments. Vertical velocity (v(x,y)) is calculated from the change in height with time, see appendix for further details.

Surface	pH	Duration (mins)	Vertical velocity (nm/sec)	Velocity error *
021	1.3	425.5	3.3×10^{-3}	8.3×10^{-5}
	2.0	470	2.4×10^{-3}	3.4×10^{-5}
	3.0	283	-9.5×10^{-3}	9.7×10^{-5}
	4.0	398.5	-2.5×10^{-4}	5.6×10^{-5}
		398.5	1.6×10^{-4}	1.4×10^{-4}
	5.9	416.5	-1.9×10^{-4}	6.3×10^{-5}
		416.5	8.9×10^{-4}	1.1×10^{-4}
010	1.0	175	-2.3×10^{-3}	1.3×10^{-5}
	2.1	500	-1.0×10^{-3}	2.9×10^{-5}
	3.0	497	-4.4×10^{-4}	3.3×10^{-5}
	4.0	443	-3.6×10^{-4}	2.6×10^{-5}
	5.9	500	-9.3×10^{-5}	1.6×10^{-5}
110	1.0	496	-2.6×10^{-3}	2.8×10^{-5}
	5.9	250	5.9×10^{-4}	1.7×10^{-5}

*calculated from standard error of the linear regression

Table 2. Comparison of dissolution flux rates, calculated from the - v(x,y) rates, and literature values.

Surface	pH	Dissolution rate * (mol/cm^2/s)	Rate (-log R)	Rate from literature† (-log R_{Si})
021	3	2.16×10^{-11}	10.67	11.97
	4	5.62×10^{-13}	12.25	12.69
	5	4.23×10^{-13}	12.37	12.98
010	1	5.19×10^{-12}	11.29	11.23
	2	2.73×10^{-11}	11.56	11.70
	3	1.00×10^{-12}	12.00	11.97
	4	8.18×10^{-13}	12.09	12.69
	5	2.11×10^{-13}	12.67	12.98
110	1	5.89×10^{-12}	11.22	11.23

*Rate conversion based on molar volume of Sapat olivine 4.39×10^{-5} m^3/mol.
†from Pokrovsky and Schott (2000) for ground olivine.

617 **Appendix**

618 Phase-Shift Interferometry measurements and data reduction

619 Figure A1. Phase-shift interferometry. (a) Phase-shift interferometer set up and sample cell, top
620 and side view. (b) Example phase image from the (010) surface. Insert shows the height profile
621 along the yellow line as calculated from the interference fringes. (c) Time-space diagram of the
622 yellow horizontal line in (b). (d) Change in height plotted against time for surface points, where
623 the point for E is represented by the vertical yellow line in (d).

624 Interferometry is a well established technique that is based on the principle of superposition,
625 where two waves with the same frequency combine to form constructive or destructive
626 interference. In situ interferometry, such as phase-shift interferometry used in this study, uses
627 laser or filtered light at a specific wavelength that is split into two, one beam of which is reflected
628 off a reference mirror whilst the other is reflected from a single focal plane at a mineral surface
629 (Fig. A1a). The two beams of light are then recombined to form a single beam and the
630 interference is recorded on a detector as an interferogram. Height difference on a surface or
631 changes in height due to surface retreat or advancement with time are observed as a change from
632 destructive to constructive interference, e.g. black to white in the interferogram.

633 As the direct information about changes in height can only be obtained from the shift in the
634 fringes on an interferogram (seen as a sharp change from black to white) rather than the whole
635 image, three normal interferograms were collected every 30 seconds for several hours using a
636 mega-pixel Peltier-cooled CCD camera with an acquisition rate of >1s by shifting the reference
637 mirror using a piezo actuator to 0, $2/3\pi$ and $4/3\pi$ phase positions. A phase image (Fig. A1b),
638 from which any pixel of the image can provide quantitative data, was then calculated from the

639 normal interferograms for each time step by determining the intensity of the fringe at a point x,y
640 (I_n) for each phase shifting position using $I_n = a(x,y) + b(x,y)\cos[\varphi(x,y) + \delta_n]$.

641 Where a is the background, b the amplitude of the fringe wavelet, φ the phase and δ_n the phase
642 shift for position n. The intensity from the three interferograms was then combined by cancelling
643 the other independent variables at each intensity of the conventional interferogram to produce the
644 contrast in the phase image, ϕ, using

645 $$\phi(x,y) = \arctan\left(\frac{\sqrt{3}[I_3(x,y) - I_2(x,y)]}{2I_1(x,y) - I_2(x,y) - I_3(x,y)}\right).$$

646 In the phase image (Fig. A1b) the change in fringe contrast from dark to light is due to changes in
647 height at the surface.

648 The interferometer is isolated from external vibrations by an air-suspended optical table and is
649 located in a temperature controlled clean-room, however, the sensitivity of the measurements to
650 other disturbances such as stage vibration, cell distortion etc. means an internal reference surface
651 was required. Gold nanoparticles were deposited on the surface as a suspension in deionized
652 water followed by fast drying of the sample so that the nanoparticles stuck to the surface. The
653 stability of the nanoparticles was evident from their ability to remain attached to the surface
654 during the flow-through experiments and their effectiveness as reference material in previous
655 studies (van Driessche et al., 2011). Vertical movement recorded by these particles during the
656 measurements was subtracted from the vertical movement of the surface to reduce the influence
657 of disturbances. During data analysis several different gold particles were examined to ensure
658 that the gold nanoparticles remained fixed during the experiment and therefore height oscillations

659 due to variations in temperature etc. were subtracted efficiently. The gold particle that produced
660 the minimal amount of noise in the corrected data was chosen for further data analysis.

661 After being corrected for drift, the acquired data was batch processed as described by Satoh et al.
662 (2007) to produce time-space diagrams of the change in grayscale intensity (*I*) with time along a
663 specific line in the phase image (Fig. A1c). Due to the monochromatic processing of the data the
664 raw data files were converted from a 24-bit bitmap file format to an 8-bit grayscale image
665 resulting in contrast values between 0 and 255 in the images. Changes in grayscale intensity (Δz)
666 at a specific point with time were taken directly from the time-space diagrams taking the
667 refractive index of the solution (n_r) into account using

668 $$\nu(x,y) = \frac{\Delta z(x,\mathrm{y})}{\Delta t} = \frac{\lambda_{522}}{2n_r} \times \frac{\Delta I(x,y)}{255}$$

669 (Fig. A1d, Table 1) and plotted as a graph to determine the vertical velocity $\nu(x,y)$.

670 The velocity of vertical retreat *v(x,y)* was translated into the more typical dissolution rates
671 (mol/cm^2/s) using rate= -ν(x,y)/V_m (Table 2), where V_m is the molar volume of forsteritic olivine
672 (4.39×10^{-5} m^3/mol) taken from the RRUFF database for Sapat olivines (RRUFF ID R060551).
673 The vertical retreat rates were normalized to step density, surface slope, by calculating the step
674 retreat using ν_{step} = -ν(x,y)/tanθ, where *v(x,y)* is the vertical velocity and Θ the measured angle of
675 the surface slope.

1. (a)

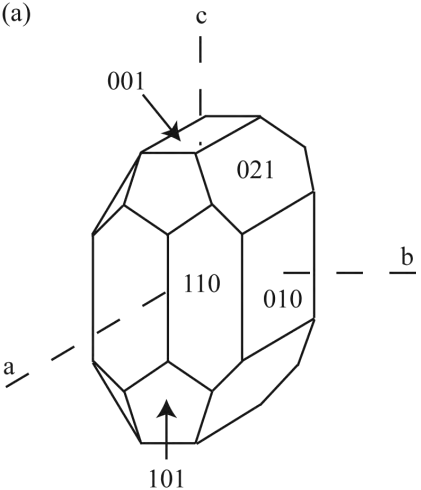

(b)

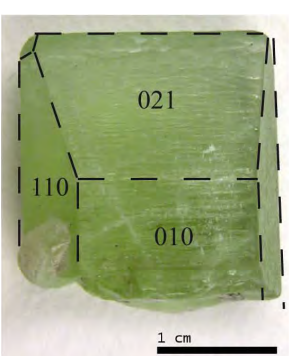

2. (a)

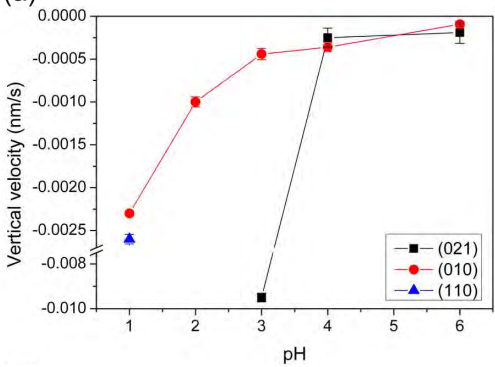
Vertical velocity (nm/s)
0.0000
-0.0005
-0.0010
-0.0015
-0.0020
-0.0025
-0.008
-0.010
1
2
3
4
5
6
pH
(021)
(010)
(110)

(b)

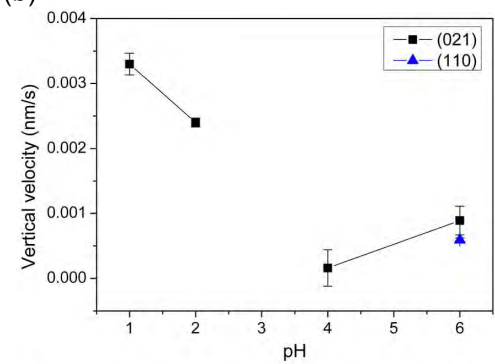
Vertical velocity (nm/s)
0.004
0.003
0.002
0.001
0.000
1
2
3
4
5
6
pH
(021)
(110)

(c)

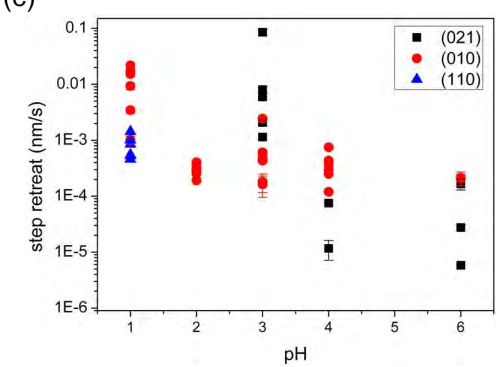
step retreat (nm/s)
0.1
0.01
1E-3
1E-4
1E-5
1E-6
1
2
3
4
5
6
pH
(021)
(010)
(110)

3.

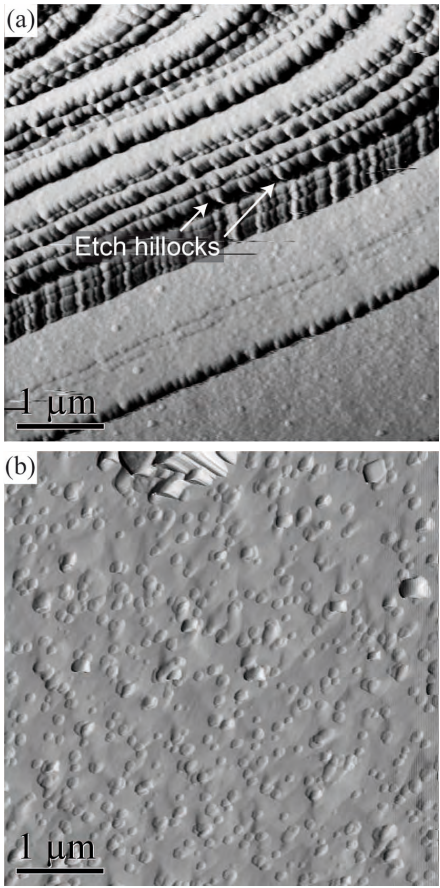

4.

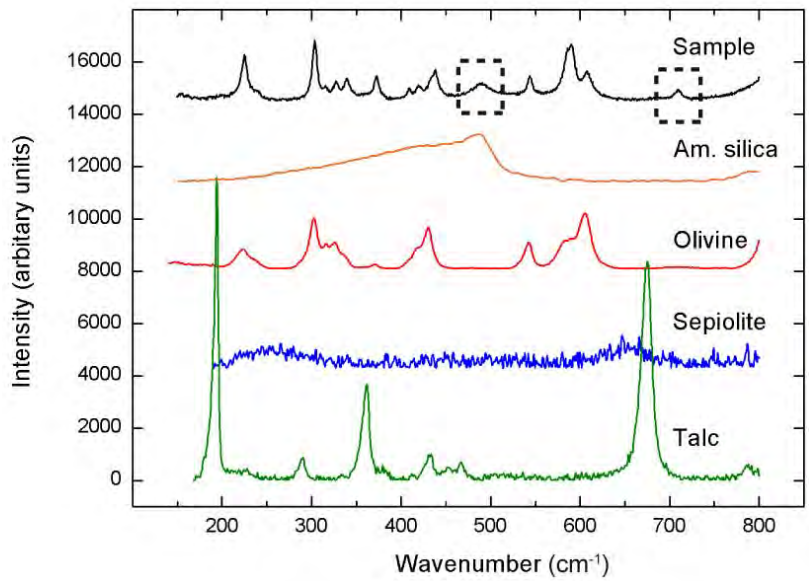
Sample
Am. silica
Olivine
Sepiolite
Talc
Intensity (arbitary units)
Wavenumber (cm-1)
16000
14000
12000
10000
8000
6000
4000
2000
0
200
300
400
500
600
700
800

5.

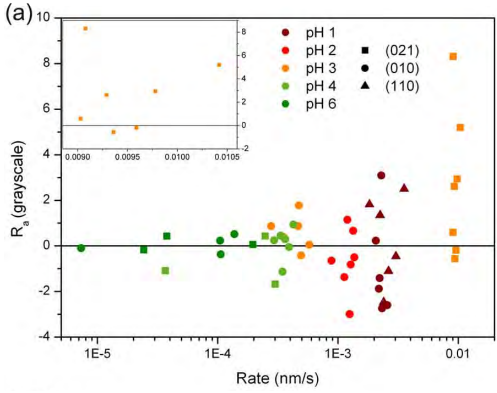
(a)
pH 1
pH 2
pH 3
pH 4
pH 6
(021)
(010)
(110)
R_a (grayscale)
Rate (nm/s)
1E-5
1E-4
1E-3
0.01

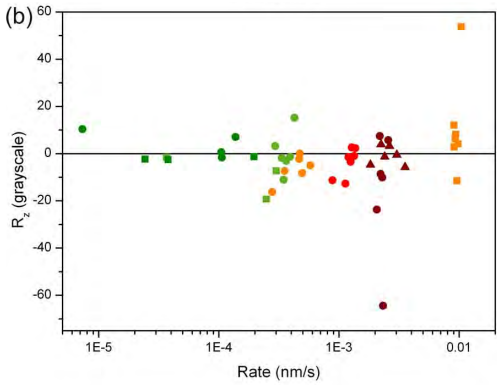
(b)
R_z (grayscale)
Rate (nm/s)
1E-5
1E-4
1E-3
0.01

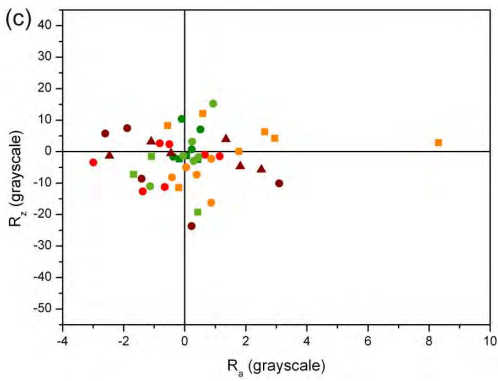
(c)
R_z (grayscale)
R_a (grayscale)

6.

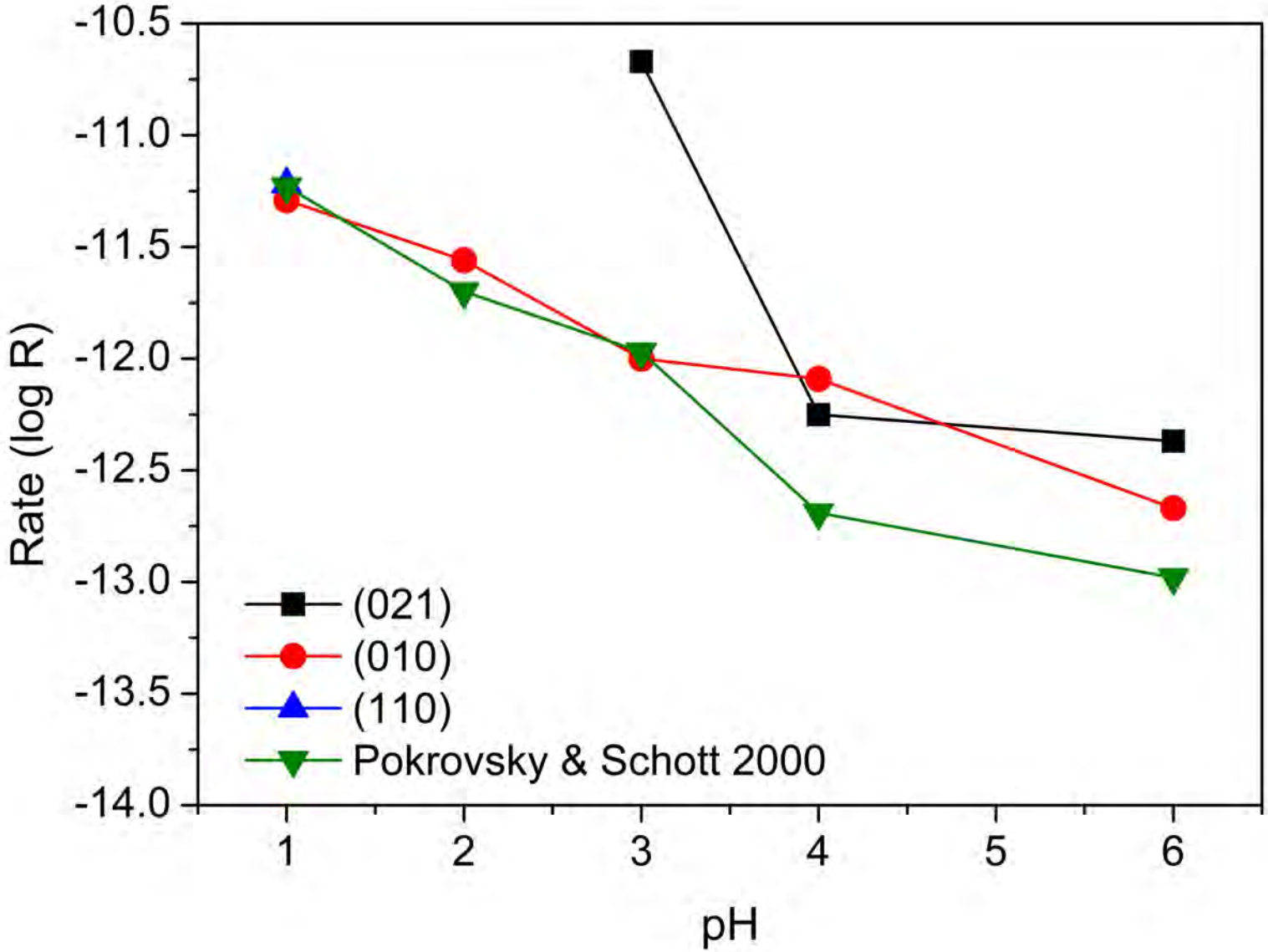
-10.5
-11.0
-11.5
-12.0
-12.5
-13.0
-13.5
-14.0
Rate (log R)
1
2
3
4
5
6
pH
(021)
(010)
(110)
Pokrovsky & Schott 2000

7.

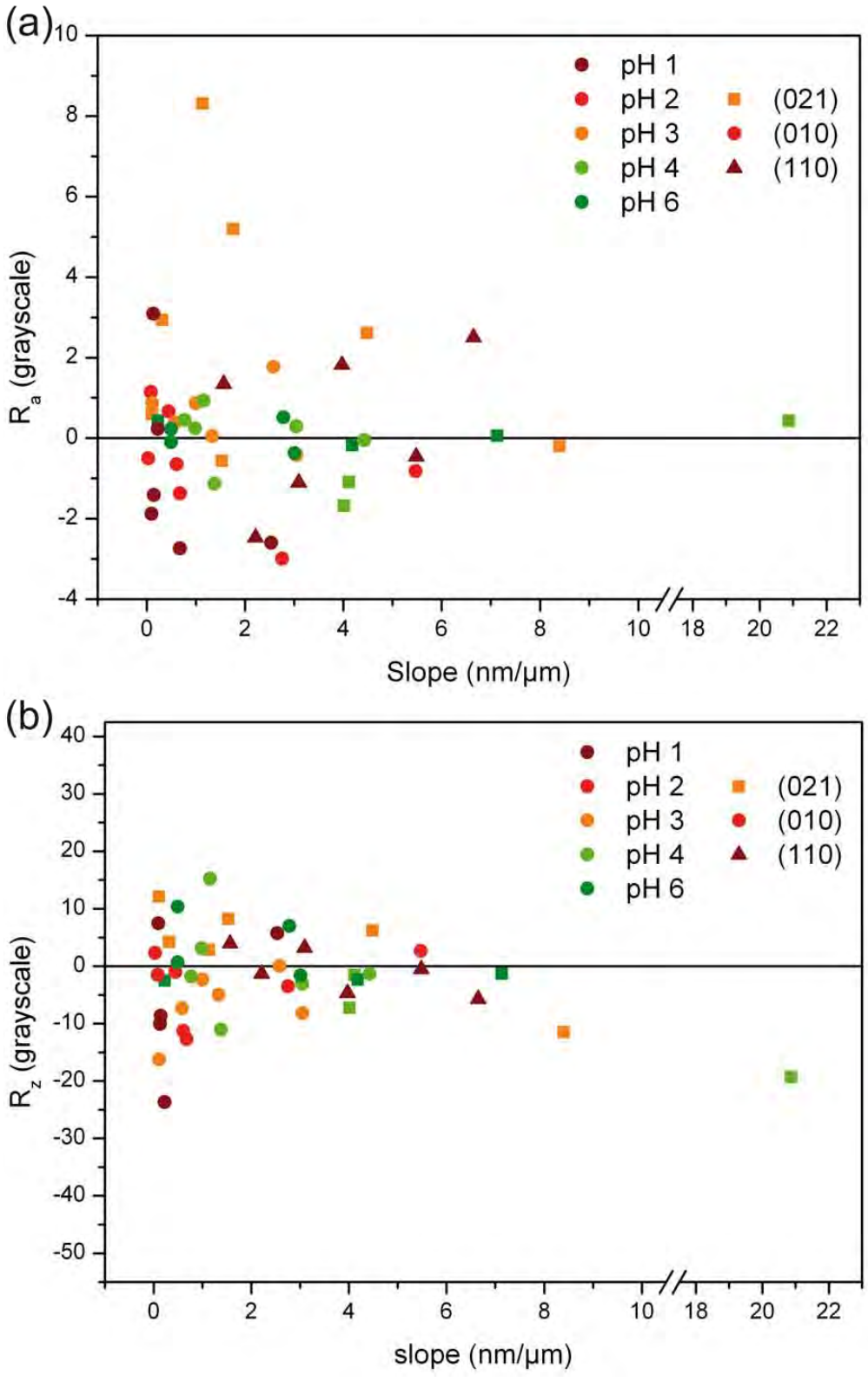
(a)
pH 1
pH 2
pH 3
pH 4
pH 6
(021)
(010)
(110)
R_a (grayscale)
Slope (nm/μm)
(b)
pH 1
pH 2
pH 3
pH 4
pH 6
(021)
(010)
(110)
R_z (grayscale)
slope (nm/μm)

A1

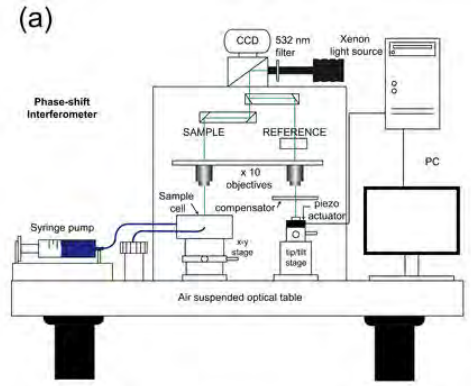
(a)
CCD
532 nm filter
Xenon light source
Phase-shift Interferometer
SAMPLE
REFERENCE
PC
x 10 objectives
Sample cell
compensator
piezo actuator
Syringe pump
x-y stage
tip/tilt stage
Air suspended optical table

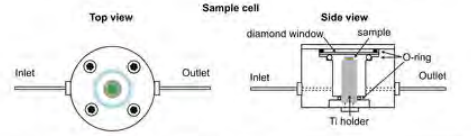
Top view
Sample cell
Side view
diamond window
sample
O-ring
Inlet
Outlet
Inlet
Outlet
Ti holder

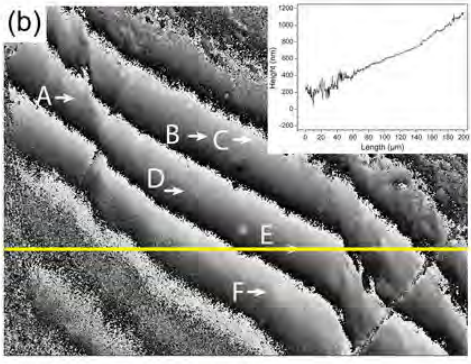
(b)
A
B
C
D
E
F
Height (nm)
Length (μm)

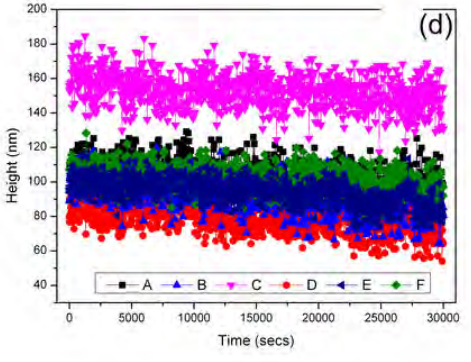
(d)
Height (nm)
Time (secs)
A
B
C
D
E
F

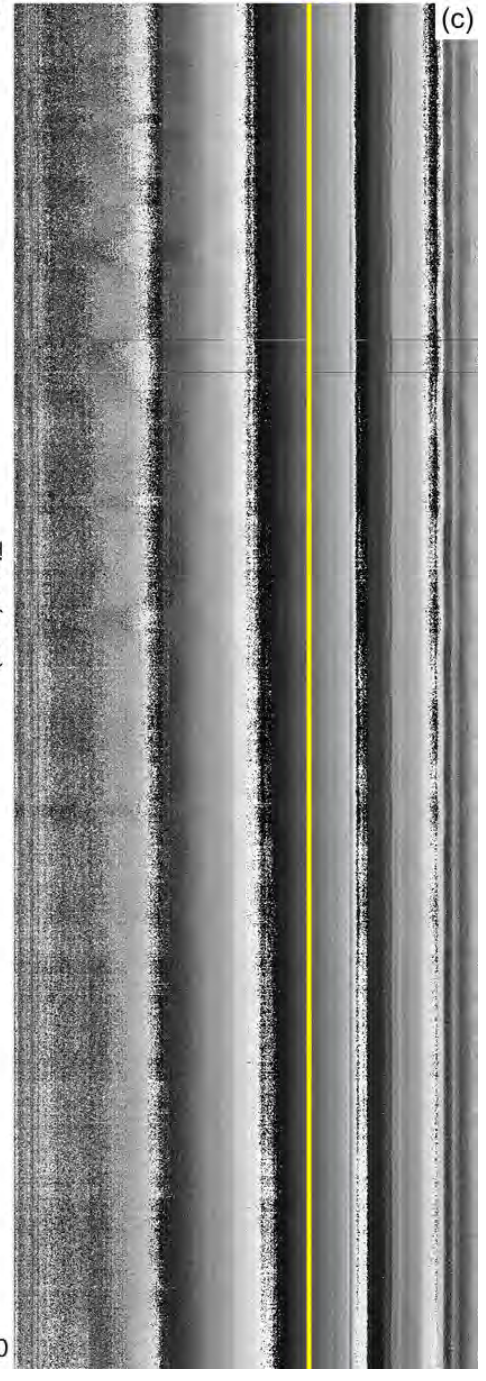
0
Time (secs)
60,000
(c)